Yu She[1,2]
Department of Mechanical and Aerospace Engineering,
The Ohio State University,
Columbus, OH 43210
e-mail: she.22@osu.edu

Hai-Jun Su
Professor
Fellow ASME
Department of Mechanical and Aerospace Engineering,
The Ohio State University,
Columbus, OH 43210
e-mail: su.298@osu.edu

Deshan Meng[3]
Department of Mechanical and Aerospace Engineering,
The Ohio State University,
Columbus, OH 43210
e-mail: meng.deshan@sz.tsinghua.edu.cn

Cheng Lai[4]
Department of Mechanical and Aerospace Engineering,
The Ohio State University,
Columbus, OH 43210
e-mail: lai@tamu.edu

Design and Modeling of a Continuously Tunable Stiffness Arm for Safe Physical Human–Robot Interaction

To reduce injury in physical human–robot interactions (pHRIs), a common practice is to introduce compliance to joints or arm of a robotic manipulator. In this paper, we present a robotic arm made of parallel guided beams whose stiffness can be continuously tuned by morphing the shape of the cross section through two four-bar linkages actuated by servo motors. An analytical lateral stiffness model is derived based on the pseudo-rigid-body model and validated by experiments. A physical prototype of a three-armed manipulator is built. Extensive stiffness and impact tests are conducted, and the results show that the stiffness of the robotic arm can be changed up to 3.6 times at a morphing angle of 37 deg. At an impact velocity of 2.2 m/s, the peak acceleration has a decrease of 19.4% and a 28.57% reduction of head injury criteria (HIC) when the arm is tuned from the high stiffness mode to the low stiffness mode. These preliminary results demonstrate the feasibility to reduce impact injury by introducing compliance into the robotic link and that the compliant link solution could be an alternative approach for addressing safety concerns of physical human–robot interactions. [DOI: 10.1115/1.4044840]

Keywords: compliant mechanisms, mechanism design, robot design, tunable stiffness arm, physical human–robot interactions

1 Introduction

Co-robots [1] have been used in various environments: exoskeletons as human power amplifiers [2], haptic devices in virtual reality environments [3], rehabilitation [4,5], and assistive devices in manufacturing [6]. Since humans and robots have complementary strengths, co-robots are particularly needed in accomplishing difficult low-volume assembly tasks [7] in which human–robot collaboration is required. However, before co-robots can be pervasively used to work side by side with human workers, the issue of safety [8] must be addressed.

To evaluate the injury severity of the impact, several safety criteria, such as head injury criteria (HIC), Gadd Severity Index, the Thoracic Trauma Index, the 3 m criterion, and the viscous injury response, from automotive and sports industries [9,10] have been developed. A safety standard ISO10218 [11] states that one of the following requirements should be satisfied for physical human–robot interaction (pHRI): the TCP (tool center point)/flange velocity $\leq$0.25 m/s, or dynamic power $\leq$80 W, or static force $\leq$150 N. Zheng and Hemami [12] derived a mathematical model to depict external impulsive forces acting on the robotic system. She et al. [13] studied the effects of reducing impact force based on compliant joint and compliant link design. Although Gao and Wampler [14] and Haddadin et al. [15] raised doubts on HIC regarding its appropriateness, it may be still one of the most commonly used criteria to evaluate safety [16] on physical human–robot interaction.

Intuitively, a robot with a light weight and a low stiffness is relatively safe. Currently, a majority of work focuses on introducing compliance to the mechanical design, which includes three principle approaches as follows. (1) Wrap robot arms with soft materials [17] to absorb impact energy. However, it has been estimated that a PUMA robot requires a compliant cover more than 5 in. in order to keep a tolerable HIC index of 100 at a velocity of 1 m/s [18]. This solution is too bulky, hence resulting in a significantly reduced performance. (2) Employ compliant or soft materials for the structural design [19,20]. These designs have a low stiffness and hence dramatically reduce the effective inertia force. Compliant and passive (underactuated) joints are commonly used in this approach. However, the biggest challenge of this approach is the severely reduced performance. (3) The third approach is novel actuator design [21]. Design of novel actuators for co-robot focuses on reducing the inertia force of moving parts by using cable drives or pneumatic actuators [22]. However, these solutions suffer from low bandwidth and hence are limited to low performance tasks.

To gain high performance, a common solution is to use a variable stiffness actuator, which has a high stiffness in low speed and a low stiffness in high speed. For instance, COMAN (Compliant humanoid) [23] incorporates joints with variable stiffness that are actuated by passive compliance actuators based on the series elastic actuation [24] principle. Zinn et al. [18] designed a distributed macro-mini actuation, which employs a pair of two actuators for the shoulder and elbow points, generating low- and high-frequency torque components, respectively. However, the results of the impact tests from DLR lightweight robot III (LWRIII) show that introducing compliance at joints does not affect the head impact response considering the link inertia is much larger than the one of the LWRIII [25].

The aforementioned variable stiffness designs are developed based on rotary joints. Researchers also explored the variable

[1]Corresponding author.
[2]Present address: Computer Science and Artificial Intelligence Laboratory, Massachusetts Institute of Technology, Cambridge, MA 02139.
[3]Present address: Department of Automation, Graduate School at Shenzhen, Tsinghua University, Shenzhen, Guangdong 518055, China.
[4]Present address: Department of Mechanical Engineering, Texas A & M University, College Station, TX 77840.

Paper presented at 2016 ASME IDETC (Paper No. IDETC2016-59523).
Contributed by the Mechanisms and Robotics Committee of ASME for publication in the Journal of Mechanisms and Robotics. Manuscript received October 8, 2018; final manuscript received August 26, 2019; published online September 12, 2019. Assoc. Editor: Nabil Simaan.

stiffness designs for prismatic joints. Rodríguez et al. [26] designed a linear adjustable stiffness spring consisting of two pairs of leaf springs. Wu and Lan [27] proposed a linear variable stiffness mechanism by parallel connecting two lateral curved beams with an axial spring. Ayoubi et al. [28,29] developed a prismatic compliant joint that is composed of a linear spring implemented in a six-bar mechanism. However, geometric configuration of the robot may be affected when the stiffness of a prismatic joint is adjusted.

Apart from variable stiffness joints design, introducing compliance to the link is an alternative solution. López-Martínez et al. [30] designed a compliant linkage for robot safe operation. The link remains a rigid part if the joint torque is less than a threshold, but splits in two parts if the condition is not satisfied. This approach ensures intrinsically safe operation for the co-robots. Park et al. [31] and Zhang et al. [32] studied similar switch off mechanisms on flexible linkage. She et al. [33,34] proposed an inherently safe robotic arm by designing various stiffness distribution along the manipulator. However, all of these flexible link designs are passive, and their stiffness is not continuously tunable. Tunable stiffness beams have been proposed and used in a variety of applications such as legged robot [35], invasive surgery [36], and flapping-wing robot [37]. But few applications can be found on safe physical human–robot interaction. Recent research of design of robotic arm with continuously tunable stiffness includes but not limits to [38–40].

In this paper, we propose a novel flexible robotic arm with continuously tunable stiffness for safe physical human–robot interaction. The original concept was presented in Ref. [41]. The robotic arm is tuned to a stiff mode if the velocity of the end effector is relatively low (e.g., 0.2 m/s [42]), which ensures the position accuracy and force control. On the other hand, the stiffness can be tuned down if the velocity is relatively high (e.g., 4 m/s [43]) for addressing the safety concerns.

We begin this paper with an introduction of problem statement in Sec. 2. Conceptual design of the morphing arm is presented in Sec. 3. In Sec. 4, detailed actuation mechanism design is presented. A lateral stiffness model of the variable stiffness arm is derived in Sec. 5. Experiment results are presented in Sec. 6 followed by discussion in Sec. 7. Finally, conclusions are summarized in Sec. 8.

2 Problem Statement

Considering a typical rest-to-rest task, an industrial robot typically goes through the stages: acceleration, steady, and deceleration, as shown, $v(t)$, in Fig. 1. At the acceleration stage, the robot starts from a speed of 0, and the speed gradually increases until the robot reaches its maximum operation speed. Then, it keeps its maximum speed until the deceleration stage when the robot slows down and stops at the target position.

Intuitively, a high stiffness arm may cause more severe injury to the environment or operators than that with a low stiffness, given the same impact velocity. To maintain efficiency (high speed) and safety simultaneously at the steady stage, one possible solution is to reduce the arm stiffness. High stiffness is required for the initial and final stage for maximum acceleration and best positioning accuracy. Therefore, the profile of the desired stiffness of the robotic arm, $k(t)$, should be stiff-compliant-stiff as shown as the solid line in Fig. 1.

To quantitatively measure injury severity, the HIC is used here to evaluate the dynamic collision. The HIC is defined as follows [9]:

$$\mathrm{HIC}(\Delta t_{\max}) = \max_{\Delta t}\left\{\Delta t\left[\frac{1}{\Delta t}\int_{t_1}^{t_2}\hat{a}\,dt\right]^{2.5}\right\} \quad (1)$$

$$\text{subject to } \Delta t = t_2 - t_1 \le \Delta t_{\max}$$

where $\hat{a}(t)$ is the normalized acceleration of the operator's head, i.e., $\hat{a} = a(t)/g$, $a(t)$ is the actual acceleration of the head, g is the gravitational constant, and (t_1, t_2) is the maximum impact interval. $\Delta t_{\max} = 15$ ms and $\Delta t_{\max} = 36$ ms are two widely used criteria and

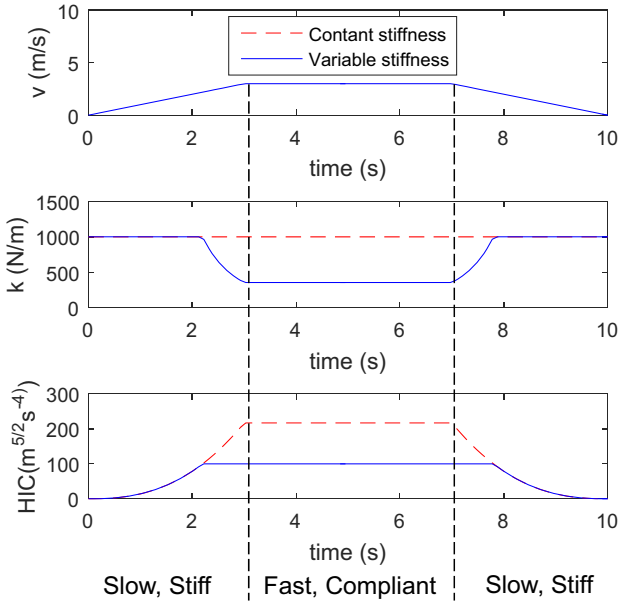

Fig. 1 A schematic view of desired profiles of velocity, stiffness, and HIC values for a typical rest-to-rest task

represented by HIC_{15} and HIC_{36}, respectively. Further detailed discussion of HIC can refer to Ref. [44], from which the limitations of the HIC to evaluate injury from the robotic system are presented as well.

The HIC distribution with respect to the constant stiffness and variable stiffness are shown as dashed line and the solid line in Fig. 1, respectively. It is observed that an appropriate dropping of the stiffness can decrease the impact effect (HIC) and hence increase the safety significantly. Therefore, the goal of this research is to design a tunable stiffness robotic arm to accommodate different velocities, hence finally to ensure the intrinsically safe operation for the manipulator.

3 Conceptual Design of the Morphing Arm

Figure 2 shows the functioning principle of the proposed robotic arm. The robotic arm is composed of two flexible arms (arm and forearm), each of which is made of two parallel flexible beams. These beams are morphed to a curved shape (stiff) by a servo motor at the start position $v(0) = 0$ for maximum acceleration. Then, they are gradually restored to the flat shape (compliant) to ensure safety when the speed reaches the maximum $v_{\max}$. At last, they are morphed back to the curved shape for maximum deceleration till they reach the end position at $v(T) = 0$.

The computer-aided design is shown in Fig. 3. The manipulator is composed of three flexible arms and three joints. The three robotic arms are forearm, arm, and trunk, while the three joints are at elbow, shoulder, and waist. The three links have the same compliant structure and provide compliance in three dimensions in space. The three joints offer the same function as the first three joints of the PUMA 560, i.e., any positions in its workspace can be reached via rotating the three joints. A counterbalance is mounted on the arm to balance the robotic arm.

All three compliant links have the same structure, which is detailed at the top of Fig. 3. Two flexible beams are inserted in the houses at both ends. The compliant beams are designed with ribs to reduce the force of morphing while maintaining relatively large lateral stiffness. A bearing frame is designed to connect the two houses between the compliant beams to support load in the vertical direction. It is a slider mechanism with two pin joints mounted on both sides of the houses. As a result, bearing frame limits the motion in the vertical direction while not affecting the lateral stiffness.

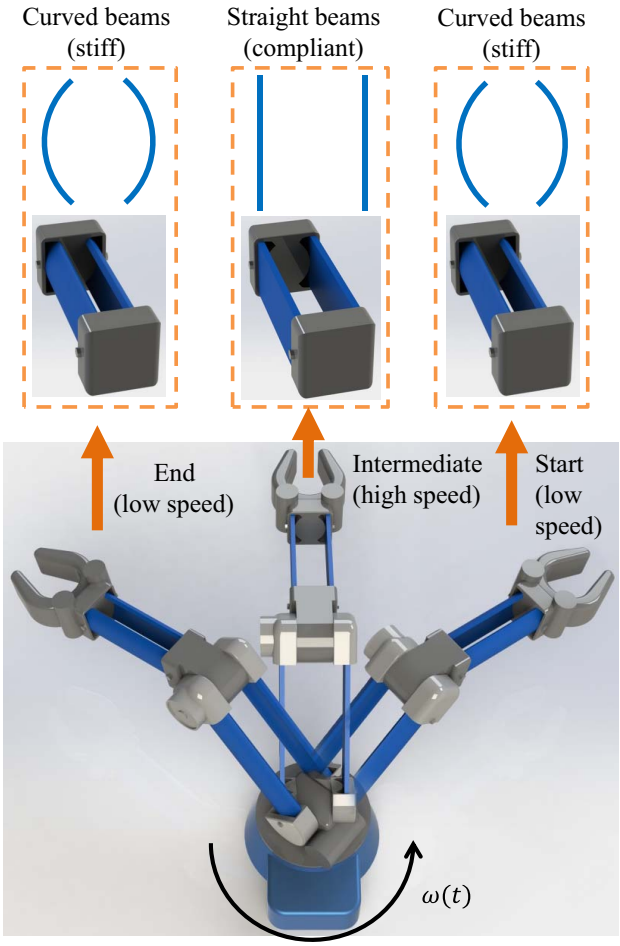

Fig. 2 A schematic view of the functioning principle of the proposed morphing arm concept. The arms are in the stiff mode when the beams are curved and in the compliant mode when the beams are flat.

The flexible beam plus the disk and the coupler form a four-bar/crank-rocker like mechanism, which is driven by a servo motor. The two flexible beams are actuated by eight pairs of four-bar linkages, with four pairs on each side. Given actuation torque of the servo motor, the flexible beam could be morphed as shown in Fig. 4. Here, the morphing angle is defined as the tip deformation angle of the flexible beam. A lager morphing angle may correspond to a stiffer arm in lateral direction.

4 Detailed Design of the Actuation Mechanism

After completion of the conceptual design, we now specify the actuation mechanism, i.e., to design the length of the linkages of the four-bar mechanisms and to determine the required torque to actuate the flexible beams.

4.1 Kinematic Analysis via Pseudo-Rigid-Body Model. Figure 5 shows the two typical positions of the actuation mechanism, which has a width of w and a height of l. The flexible beam is flat and compliant as shown in Fig. 5(*a*) and is curved and stiff as shown in Fig. 5(*b*). The flexible beam is an initially straight pinned-pinned segment, which is fixed in the middle by attaching on the houses of both ends. The couplers connect the tips of the flexible beams and a disk, and the disk is attached on servo motors to provide the input torque. Given actuation from the disk, the flexible beam deforms as a cantilever beam as shown in Fig. 5(*b*).

By symmetry, two diagonal four-bar linkages Q_a are in the same phase and the other two four-bar linkages Q_b have a different phase,

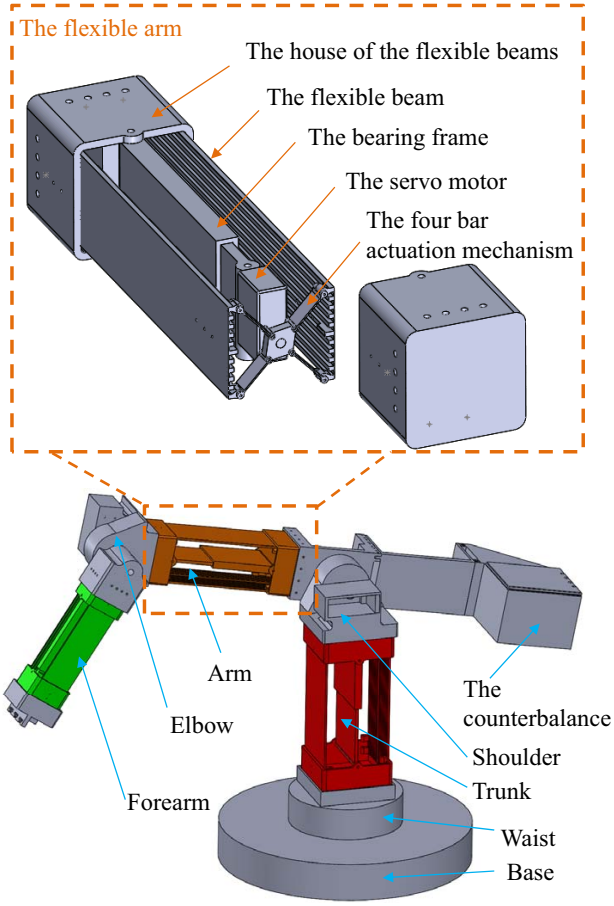

Fig. 3 The design of the proposed morphing manipulator

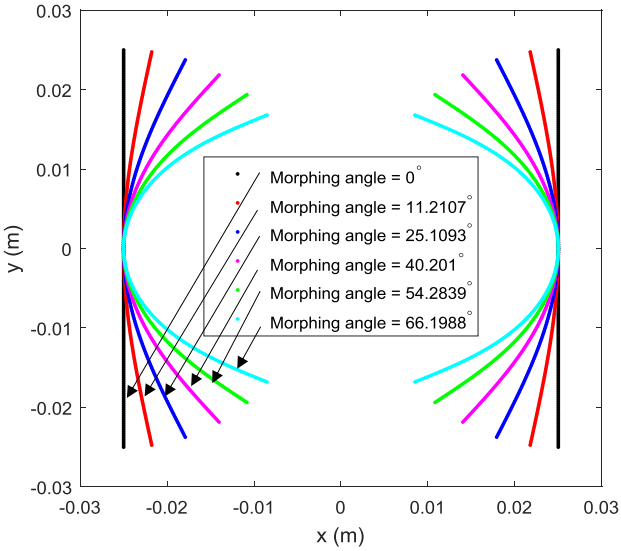

Fig. 4 The morphing shapes of the flexible beams

as shown in Fig. 5. The linkages of Q_a and Q_b can generate corresponding morphing angles of θ_{0a} and θ_{0b} (Fig. 6(*b*)), respectively. It is worth noting that the crank lengths for Q_a and Q_b on the disk, i.e., r_{2a} and r_{2b}, have different lengths, which will be discussed later in detail.

Due to similarity, we only need to analyze one four-bar mechanism, e.g., the upper right one Q_a in Fig. 5(*a*). We first convert the flexible beam into the pseudo-rigid-body (PRB) model as shown in Fig. 6(*b*). PRB model [45,46] is a simple and efficient tool for

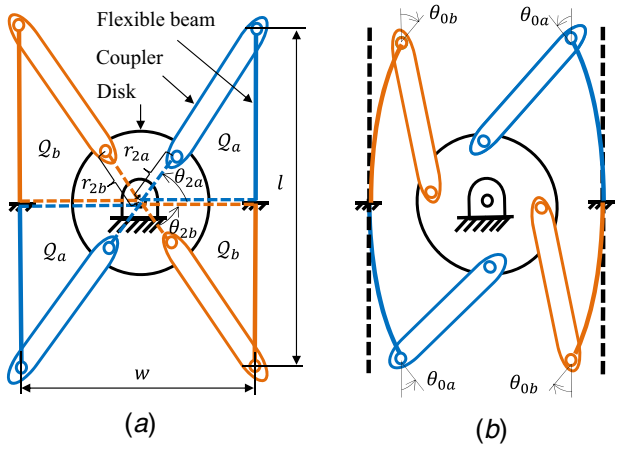

Fig. 5 (*a*) The actuation mechanism is in the flat beam shape (compliant) and (*b*) the actuation mechanism is in the curved beam shape (stiff)

modeling compliant links especially in the initial design stage, which will be used for the kinematics analysis of the flexible beam.

Assume the flexible beam has a length, height, and thickness of L, l, and t, respectively. The length of the rocker can be calculated as follows:

$$r_{4a} = r_{4b} = \frac{\gamma l}{2} \tag{2}$$

where γ is the characteristic radius factor [47]. The stiffness of the torsional spring of the cantilever beam can be calculated as follows:

$$k_z = \frac{\gamma K_\theta E I_z}{l/2} \tag{3}$$

where K_θ is the stiffness constant, E is the material modulus of the flexible beam, and I_z is the second moment of inertia calculated by $I_z = Lt^3/12$. Note the force applying to the tip of the flexible beam will be along with the direction of the coupler since it is the pinned-pinned link. Assume the coupler angle is around 45 deg with a slight variation, one can find $\gamma = 0.84$ and $K_\theta = 2.61$ according to Ref. [47].

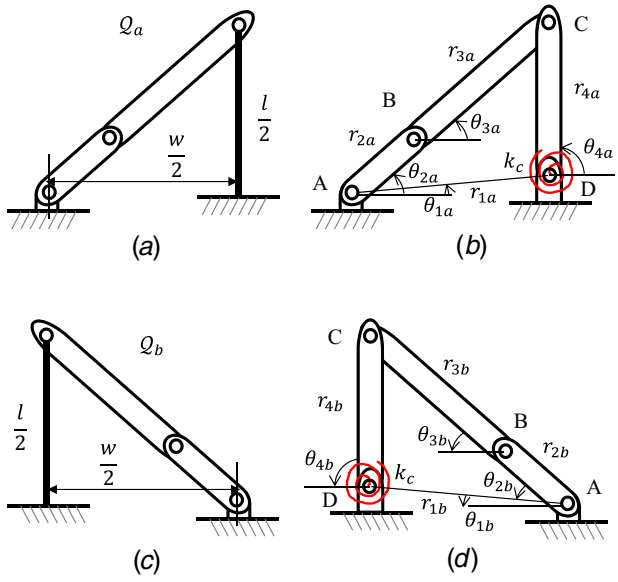

Fig. 6 (*a*) The four-bar actuation mechanism of Q_a, (*b*) the PRB model of the four-bar linkage of Q_a, (*c*) the four-bar actuation mechanism of Q_b, and (*d*) the PRB model of the four-bar linkage of Q_b

If we define the morphing angle of the entire flexible beam as Ω, it can be calculated as follows:

$$\Omega = \theta_{0a} + \theta_{0b} = c_\theta(\theta_{4a} + \theta_{4b}) \tag{4}$$

where c_θ is the parametric angle coefficient of the PRB model, which is $c_\theta = 1.25$ in this case [47]. θ_{4a} and θ_{4b} are the rocker angles for linkage Q_a and Q_b, respectively, which can be calculated by kinematic analysis of the four-bar linkages given input crank angles of θ_{2a} and θ_{2b}.

The four-bar actuation mechanism and the associated PRB model of Q_a and Q_b are shown in Fig. 6. Consider the four-bar mechanism Q_a, the dimensions of the base link r_{1a} and the rocker link r_{4a} are determined according to the size of the robot arm. In addition, we would like to design the four-bar linkage initially under a toggle position such that the flexible beams are stable in the flattened position. Therefore, some dimensions or constrains of the mechanisms can be obtained as follows:

$$\begin{cases} r_{1a} = r_{1b} = \sqrt{\dfrac{w^2}{4} + \dfrac{(l-\gamma l)^2}{4}} \\ r_{2a} + r_{3a} = r_{2b} + r_{3b} = \sqrt{\dfrac{w^2}{4} + \dfrac{l^2}{4}} \end{cases} \tag{5}$$

The initial linkage angles of the four-bar mechanism are stated as follows:

$$\begin{cases} \theta_{1a} = \theta_{1b} = \arctan\dfrac{(1-\gamma)l}{w} \\ \theta_{2a} = \theta_{3a} = \theta_{2b} = \theta_{3b} = \arctan\dfrac{l}{w} \\ \theta_{4a} = \theta_{4b} = 90\,\text{deg} \end{cases} \tag{6}$$

4.2 Length Optimization of the Four-Bar Mechanism. Ideally, we would like the flexible beams are morphed as symmetrical as possible for balance purpose, i.e., $\theta_{4a} = \theta_{4b}$ for the same input of crank angle $\theta_{2a} = \theta_{2b}$. However, this is not possible if Q_a and Q_b share the same dimensions since they are actually two different branches of a four-bar mechanism. Therefore, to achieve the symmetrical purpose, we may first choose the dimension of Q_a and then optimize dimension of Q_b by minimizing the overall difference between the two linkages, or vice versa.

The dimensions of the flexible arm refer the size of a commercial light weight robot as $w = 50$ mm and a height of $l = 50$ mm. Considering the practicality in fabrication and assembling, we specify $r_{2a} = 10$ mm and $\Omega = 37$ deg for Q_a and then we can determine all dimensions of Q_a by Eqs. (2) and (5). Note, we assume the beam morphing angle θ_0 finally is equally distributed to θ_{4a} and θ_{4b}, i.e., $\theta_{4a} = \theta_{4b} = 15$ deg at the maximum curved position according to Eq. (4). In terms of Q_b, r_{1b} and r_{4b} are also determined according to Eqs. (2) and (5), while r_{2b} and r_{3b} are to be found. Since r_{2b} and r_{3b} need to satisfy a constraint in Eq. (5), we actually have only one parameter to be explored and optimized, i.e., either r_{2b} or r_{3b}.

Here, r_{2b} is selected as the optimization subject. Consider the robot arm dimension and physical prototyping restraint, the constraint U of the length of r_{2b} is set as $0.002\,\text{m} \le U \le 0.02$ m. Given this constrain, one can plot the curve of the rocker angle versus crank angle as shown in Fig. 7. The bold line represents the curve of Q_a, which is fixed, while the thin lines represent the curves of Q_b exploring from $r_{2b} = 0.002$ m to $r_{2b} = 0.02$ m.

The goal of the optimization is to find an optimal r_{2b} such that the endpoint of r_{4b} is as close to that of r_{4a} as possible for any given crank angle of θ_{2b}, while ensuring the flexible beams on both sides being as symmetrical as possible at an arbitrary position within workspace. Consider $r_{4a} = r_{4b}$, we can convert the optimization objective from Cartesian space to joint space for the sake of convenience, i.e., given an arbitrary crank angle θ_{2b}, the rocker angle θ_{4b} should be as close as possible to θ_{4a}, and vice versa.

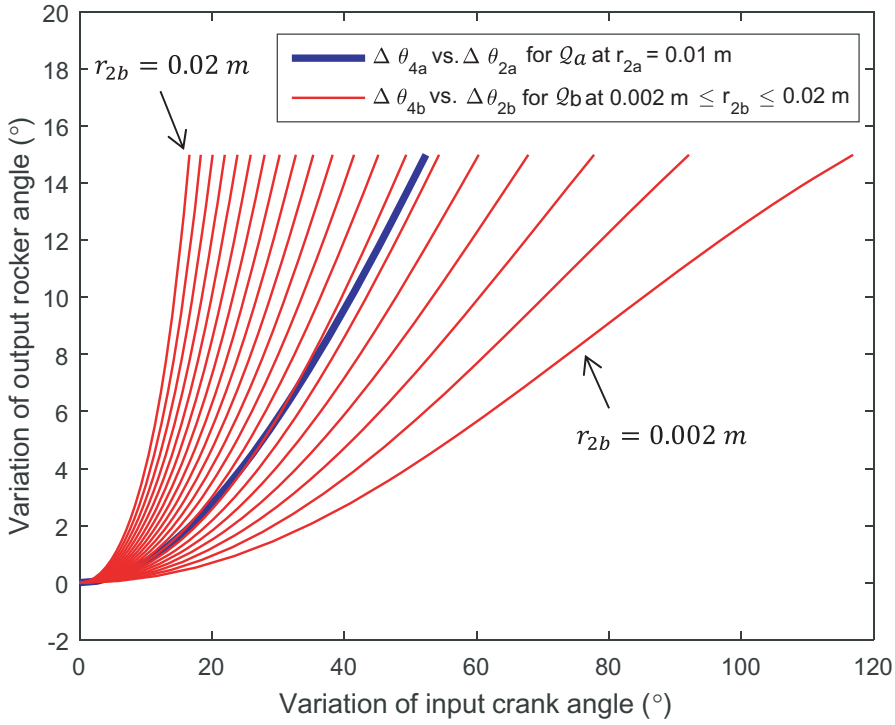

Fig. 7 The plots of the rocker angle versus the crank angle for various crank lengths $r_{2b} \in [0.002, 0.02]$ m for linkage Q_b. The thick line represents the plot for the linkage Q_a.

Observing Fig. 7, we would like the thin line as close as possible to the bold line starting from $\theta_{4b} = 0$ deg to $\theta_{4b} = 15$ deg. We then formulate the optimization problem as follows:

$$r_{2b}^* = \arg \min_{r_{2b} \text{ s.t. } U} \left(\int_0^{15\,\text{deg}} \left\| \frac{\theta_{4a}}{\theta_{2a}} - \frac{\theta_{4b}(r_{2b})}{\theta_{2b}(r_{2b}, \theta_{4b})} \right\| d\theta_{4b} \right) \tag{7}$$

where θ_{2b} is considered as a function of θ_{4b} by the kinematic analysis of the four-bar linkage [48].

It is found that $r_{2b} = 7.8$ mm is the optimal solution. The 3D printer used in this work may be not accurate enough to ensure the dimension. For fabrication convenience, the length is rounded to 8 mm, which is a close integer to the optimal one.

We then define the joint error as follows:

$$\epsilon_j = \frac{|\theta_{4a} - \theta_{4b}|}{\max(\theta_{4b})} \times 100\% \tag{8}$$

Consider the Cartesian space, we flip Q_b and place it on top of Q_a, and we use (x_{Ca}, y_{Ca}) and (x_{Cb}, y_{Cb}) to represent the position of the endpoint of the rocker (point C as shown in Fig. 6) for Q_a and Q_b, respectively. Then, we define the position error as follows:

$$\epsilon_c = \frac{\sqrt{(x_{Ca} - x_{Cb})^2 + (y_{Ca} - y_{Cb})^2}}{r_{4b}} \times 100\% \tag{9}$$

With the rounded rocker length $r_{2b} = 8$ mm, it is found that the joint error $\epsilon_j < 1.5\%$ and position error $\epsilon_c < 2.5\%$.

Given the optimized length of r_{2b}, the length of the coupler linkage of Q_b can be obtained as 27 mm. The dimensions of the linkages and the initial linkage angles of the four-bar mechanisms are summarized as shown in Tables 1 and 2, respectively.

4.3 Kinematics Simulation and Torque Determination. After quantifying the dimensions of the four-bar linkage, the kinematics simulation of the entire actuation process of the four-bar linkages are presented in Fig. 8. As one can see, the motion of the diagonal four-bar pairs has identical phase, and the motion of the output link of the adjacent pairs is very close to each other.

Table 1 Dimensions of the four-bar mechanisms

Q_a	Value (mm)	Q_b	Value (mm)
r_{1a}	25.3	r_{1b}	25.3
r_{2a}	10	r_{2b}	8
r_{3a}	25	r_{3b}	27
r_{4a}	21.3	r_{4b}	21.3

Table 2 Initial linkage angles of the four-bar mechanisms

Q_a	Value (deg)	Q_b	Value (deg)
θ_{1a}	8.5	θ_{1b}	8.5
θ_{2a}	45	θ_{2b}	45
θ_{3a}	45	θ_{3b}	45
θ_{4a}	90	θ_{4b}	90

With the kinematics relationships, one can find the required motor torque to drive the flexible beams:

$$\tau_m = 2k_z\theta_{4a}\frac{\partial\theta_{4a}}{\partial\theta_{2a}} \tag{10}$$

$$\frac{\partial\theta_{4a}}{\partial\theta_{2a}} = \frac{r_{2a}}{r_{4a}}\frac{r_{1a}\sin\theta_{2a} + r_{4a}\sin(\theta_{2a} - \theta_{4a})}{r_{2a}\sin(\theta_{2a} - \theta_{4a}) + r_{1a}\sin\theta_{4a}} \tag{11}$$

5 Stiffness Modeling of the Morphing Arm

After determining the dimensions, kinematics, and actuation torques of the four-bar mechanism, we now start to model the lateral stiffness of the morphing arm.

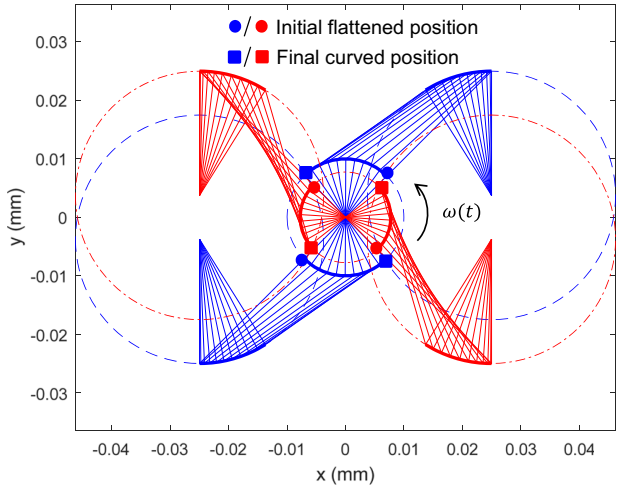

Fig. 8 Kinematics simulation of the actuation process

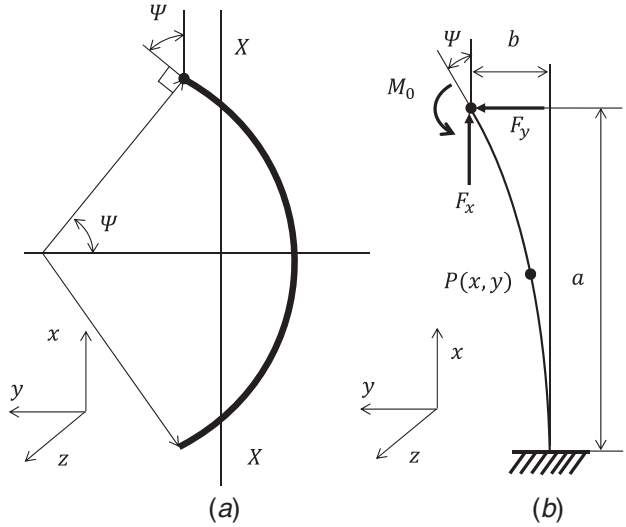

Fig. 9 (*a*) Morphing shape of the flexible beam and (*b*) the cantilever beam model considering half of the flexible beam

5.1 Static Model for the Morphing Shape. Given an actuation torque from the servo motor, the flexible beams from the flattened shape become a curved shape. It is intuitive that the lateral stiffness relies on the shape of the flexible beam. The aforementioned PRB model is convenient for determining the geometric dimensions, kinematics, and required torques of the actuation mechanism. However, it cannot provide the exact beam shape, which may be required to model the lateral stiffness. Therefore, we need to derive the static model to obtain the beam shape under large deformations.

Given an actuation from the servo motor, the flexible beam may deform as shown in Fig. 9(*a*). The flexible beam is actually a pinned-pinned segment and fixed in the middle. One can take half of the beam and model it as a cantilever beam as shown in Fig. 9(*b*).

Assume external force F_x, F_y, and moment M_0 are applied at the tip of the cantilever beam, and it is balanced with a tip displacement of (a, b) and morphing angle Ψ. Note Ψ is the tip angle from the half of the flexible beam. Here, the entire morphing angle of the flexible beam is as follows:

$$\Omega = 2\Psi \tag{12}$$

The moment at arbitrary position $P(x, y)$ can be calculated by

$$M(x, y) = F_x(y - b) + F_y(a - x) + M_0 \tag{13}$$

Consider thin flexible beams are used in this study, we may apply the Bernoulli–Euler equation here:

$$\frac{d\theta}{ds} = \frac{M(x, y)}{EI_z} \tag{14}$$

where s is any point on the cantilever beam with $0 < s < l/2$ and $d\theta/ds$ is the rate of change in angular deflection along the beam. Equation (14) takes derivative to s and we have

$$\frac{d^2\theta}{ds^2} = \frac{1}{EI_z}(F_x \sin\theta(s) - F_y \cos\theta(s)) \tag{15}$$

where θ is the beam angle along the beam. With the initial condition $\theta(0) = 0$ and $\theta'(L) = M_0/EI_z$, one can find the lateral displacement b and morphing angle Ω of the cantilever beam.

Remember the key point to calculate the morphing shape is to obtain the second moment of inertia of I_{XX}, where XX is the centroid axis of the deformed flexible beam as shown in Fig. 9(*a*). The position of the centroid axis can be calculated by

$$\bar{y} = \frac{\int_A y dA}{A} \tag{16}$$

where A is the cross section of the flexible beam of $A = lt/2$. Note the flexible beam is actually two sets of the cantilever beam, and then, the second moment of inertia of the deformed flexible beam can be calculated by

$$I_{XX} = 2\iint_A \bar{y}^2 dA \tag{17}$$

Given external forces or moment, we could calculate the beam morphing angle Ω from Eq. (15) and I_{XX} from Eq. (17). A specific shape corresponds to a unique morphing angle Ω and a unique second moment of inertia I_{XX}. We consider a simple case that the mapping from Ω to I_{XX} is bijective, and then, a morphing angle Ω may correspond to a unique second moment of inertial $I_{XX}(\Omega)$.

5.2 Lateral Stiffness Modeling With Pseudo-Rigid-Body Model. The flexible arm is essentially a compliant parallelogram mechanism as shown in Fig. 10(*a*), which can be treated as a fixed-guided PRB model as shown in Fig. 10(*b*). Given a lateral force F at

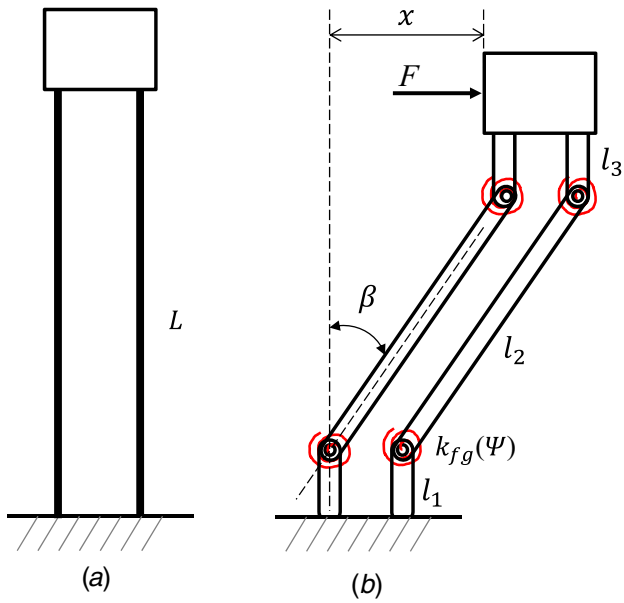

Fig. 10 (*a*) The compliant parallelogram mechanism and (*b*) the fixed-guided PRB model for lateral stiffness

the stage, it will have a lateral displacement of x with a deflection angle β as shown in Fig. 10(*b*). The length of each link of the PRB model is l_1, l_2, and l_3 and can be calculated as follows:

$$\begin{cases} l_1 = l_3 = (1-\gamma)L/2 \\ l_2 = \gamma L \end{cases} \tag{18}$$

The four torsional springs of the PRB model are identical, and the stiffness of each torsion springs of the fixed-guided PRB model can be calculated by

$$k_{fg}(\Omega) = \frac{2\gamma K_\theta E I_{xx}(\Omega)}{L} \tag{19}$$

Note, in this paper, the continuous stiffness variation is achieved by deforming the flexible beam with a morphing angle Ω, i.e., tuning the second moment of inertia $I_{xx}(\Omega)$.

With four torsional springs, the potential energy can be calculated by

$$V = 2k_{fg}(\Omega)\beta^2 \tag{20}$$

By virtual work principle, we have

$$F\delta x - \frac{dV}{d\beta}\delta\beta = 0 \tag{21}$$

Then, we can determine the relationship between the lateral force and the deflection angle as follows:

$$F = \frac{4k_{fg}(\Omega)\beta}{\gamma L \cos\beta} \tag{22}$$

The lateral stiffness of the compliant arm can be calculated by

$$K_\delta(\Omega, \beta) = \frac{dF}{dx} = \frac{4}{\gamma^2 L^2} k_{fg}(\Omega) \frac{(\cos\beta + \beta \sin\beta)}{\cos^3\beta} \tag{23}$$

According to our later experimental validation, it is found that the lateral stiffness model based on the aforementioned PRB model actually is not sufficiently accurate. The major issue is that the PRB model assumes that the flexible beams are ideally fixed on both end houses. In this case, however, this assumption may not be satisfied. As we mentioned early, the couplers connect the flexible beams and the disks, and the disks are attached on servo motors. Since the flexible beams are deformable, they are not perfectly fixed on the houses. As a matter of fact, the rigidity of the connection between the flexible beams and the houses depends on the stall torque of the servo motor. To improve the accuracy of the lateral stiffness model, we model the compliance of the connection part between the flexible beams and the houses with four identical torsions springs.

5.3 The Improved Lateral Stiffness Model. In addition to the original PRB model of the compliant parallelogram mechanism, we assume the compliance of the connection parts are lumped by four identical torsional spring k_b, and the improved lateral stiffness model is described in Fig. 11. Given a lateral force F, both l_1 and l_3 deforms with β_1 in addition to l_2 deforming with β_2.

The lateral displacement can be calculated by

$$x = (1-\gamma)L \sin\beta_1 + \gamma L \sin(\beta_1 + \beta_2) \tag{24}$$

According to the free body diagram, one can find the relationship of lateral force and deformation angles as follows:

$$F = 4k_b\beta_1 \frac{1}{(1-\gamma)L\cos\beta_1 + \gamma L\cos(\beta_1+\beta_2)} \tag{25}$$

$$F = \frac{4k_{fg}(\Omega)\beta_2}{\gamma L} \frac{1}{\cos(\beta_1+\beta_2)} \tag{26}$$

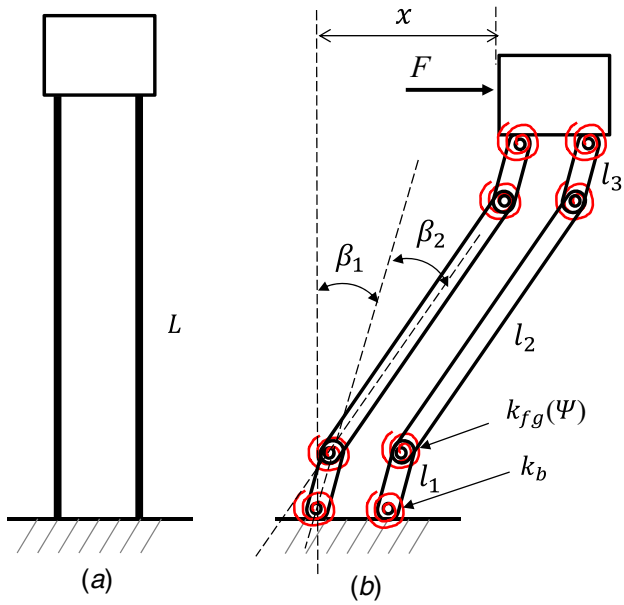

Fig. 11 (*a*) The compliant parallelogram mechanism and (*b*) the improved lateral stiffness model

Substituting Eq. (26) in (25) to eliminate the lateral force, one can find the relationship of the deformation angles as follows:

$$\frac{\beta_1}{\beta_2} = \frac{k_{fg}(\Omega)}{k_b}\left[\left(\frac{1-\gamma}{\gamma}\right)\frac{\cos\beta_1}{\cos(\beta_1+\beta_2)} + 1\right] \tag{27}$$

Given a lateral force F, one can find the deformation angles β_1 and β_2 with any two equations from Eqs. (25) to (27). Then, one can find the lateral displacement x according to Eq. (24). With the lateral force and the solved lateral displacement, the lateral stiffness of the compliant parallelogram mechanisms with fixture compliance can be obtained.

6 Experimental Testings

A three-armed robotic manipulator with tunable stiffness is fabricated by a 3D printer[5] with acrylonitrile butadiene styrene (ABS) plastic material. A single flexible robotic arm is shown in Fig. 12(*a*), and the three-armed robotic manipulator is shown in Fig. 12(*b*). In Fig. 12(*a*), two servo motors[6] are placed on both sides of the robot arm to morph the flexible beam to control the arm stiffness. In Fig. 12(*b*), three flexible arms are assembled together to provide compliance in three dimensions. The rotation from the waist, shoulder, and wrist enable the end of the forearm to reach any position in its workspace. A DC motor[7] is placed at the waist, and two ultra high torque servo motors[8] are placed at the shoulder and wrist.

The stiffness tests are conducted after the robotic link are fabricated and assembled. The experiment setup of the stiffness test is as shown in Fig. 13. The morphing arm is clamped to a fixture at one end on a table. A high-resolution force sensor[9] (0.002 N resolution) is fixed on the platform of a computer numerical control (CNC) mill, and the sensor contacts the end of the flexible arm to measure the lateral force of the flexible arm at the end. A displacement sensor[10] (0.013 mm resolution) is clamped on the table to measure the displacement of the platform of the CNC mill, which

[5]Replicator+, MakerBot.
[6]HS-81, HITEC RCD USA, Inc.
[7]FR801-001, CCL Industrial Motor.
[8]HD-1235MG, Pololu.
[9]PS-2189, PASCO.
[10]PS-2204, PASCO.

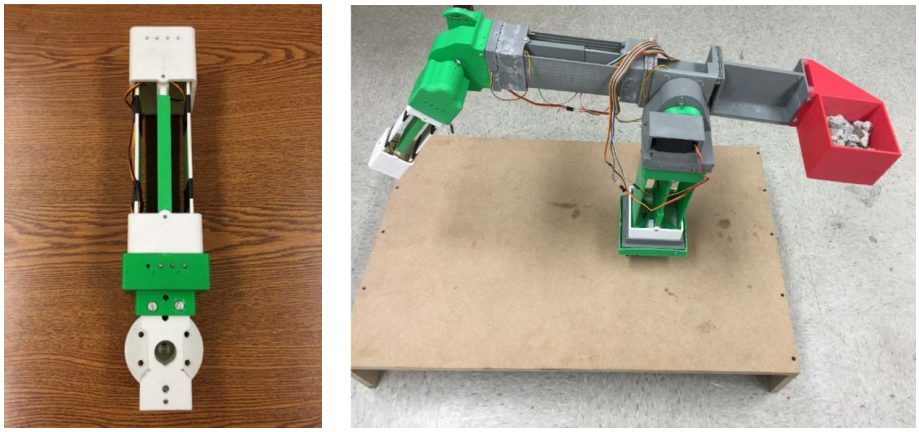

(*a*) (*b*)

Fig. 12 (*a*) The 3D printed flexible arm and (*b*) the 3D printed robotic manipulator

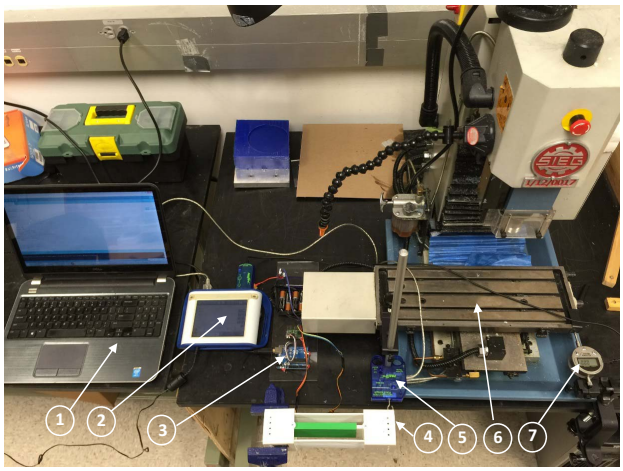

Fig. 13 The experiment setup of the stiffness test: 1, laptop; 2, data acquisition system; 3, micro-controller; 4, morphing arm; 5, force sensor; 6, CNC platform; 7, displacement sensor

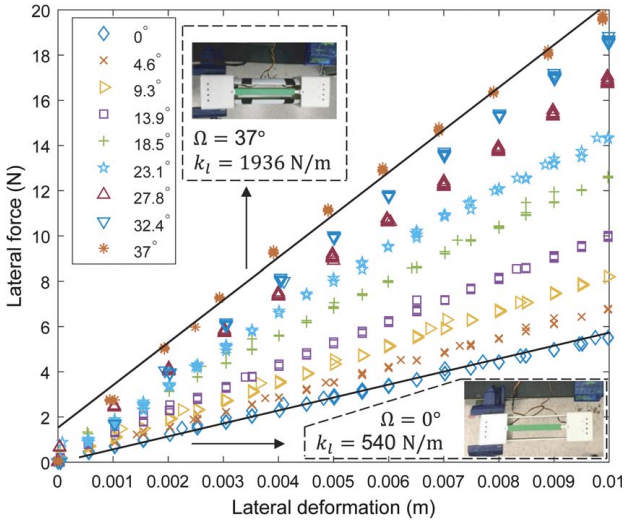

Fig. 14 The stiffness testing results

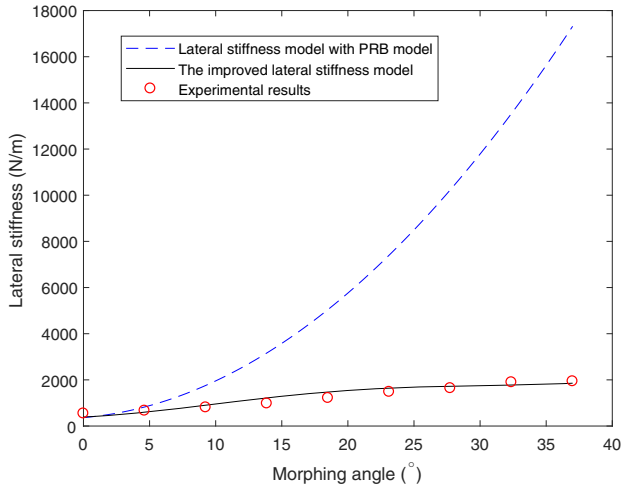

Fig. 15 Stiffness model verification

represents the deformation of the flexible arm at the end. The CNC mill is used here to generate precise, repeatable, and motorized displacement. Therefore, given displacement command from the CNC mill, its platform pushes the end of the flexible arm to deform the arm, and the lateral force and lateral deformation are captured by the aforementioned sensors. A data collection and analysis device[11] is used to access data from the sensors. The motion of the platform of the CNC mill is controlled by a computer (data not shown). A laptop is used to update the program of the micro-controller. The morphing angle is driven by two servo motors, which are controlled by the micro-controller.

The stiffness testing results are shown in Fig. 14. Applying a lateral force F and reading a corresponding displacement δ from the sensors, one can calculate the lateral stiffness using $k_l = F/\delta$. In this test, different morphing angles are tested and controlled by the servo motors, and the slopes represent the arm stiffness at a specific morphing angle. The morphing angle are increased from 0 to 37 deg, and the stiffness increases from 540 N/m to 1936 N/m. The maximum stiffness at $\Omega = 37$ deg is 3.6 times of the smallest stiffness at $\Omega = 0$ deg.

We then plot the stiffness versus morphing angles in Fig. 15, where the dashed line represents the theoretical estimation of the lateral stiffness model with the PRB model, the solid line represents the theoretical estimation of the improved lateral stiffness model, and the circled line represents the experimental results.

Noteworthy, E and k_b are determined from a set of separate experimental testing. It is identified that $E = 1.2$ Gpa and $k_b = 25$ N m/rad give the minimal accumulated errors (averaged)

[11]PS-2008A, PASCO.

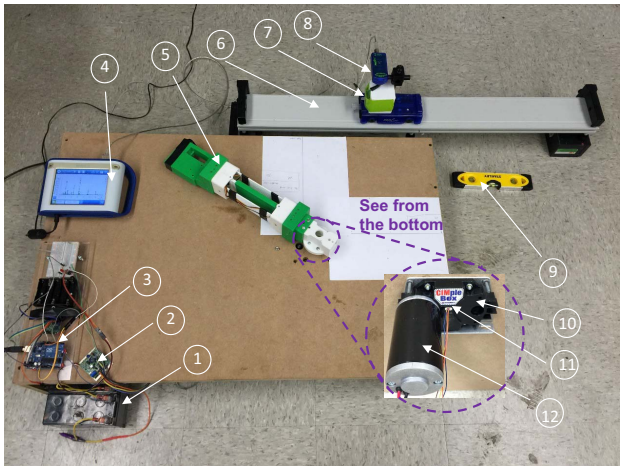

Fig. 16 The impact experiment setup: 1, power supply; 2, speed controller; 3, micro-controller; 4, data acquisition system; 5, morphing arm; 6, a frictionless slide trail; 7, force sensor; 8, acceleration sensor; 9, Stanley level; 10, gear box; 11, encoder; 12, DC motor

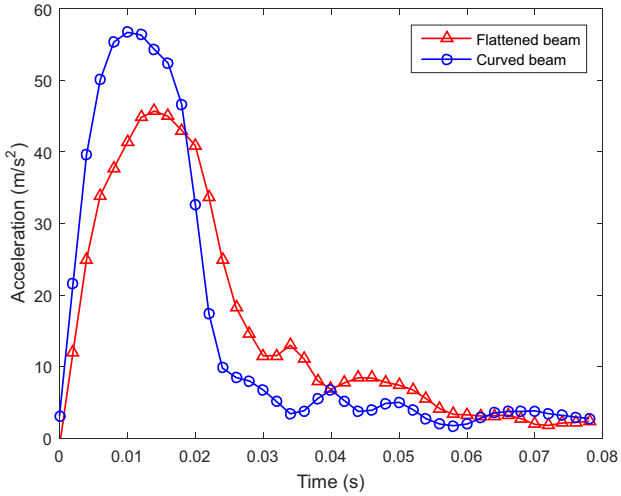

Fig. 17 Impact comparisons between the flattened beam with minimum stiffness and the curved beam with maximum stiffness

between the results from the improved model and the separate testing data. We then fixed these parameters for the improved model.

It is observed that the PRB-based theoretical model cannot predict the experiment results, while the simulation data by the improved model agree with the experimental results with a maximum error of 12.78%. Note, the ultimate case of the improved lateral stiffness model is that k_b is infinite large, which results in the solid line coinciding with the dashed line. That is to say, if the rigidity between the flexible beams, the couplers, the disk, and the servo motor (k_b) can be improved significantly, the actual lateral stiffness of the arm can be increased significantly as well. However, the mobility of the four-bar mechanism requires flexibility for operation to morph flexible beam shapes. Therefore, there is a trade-off between the large stiffness variation and easy operation of the four-bar linkage.

After the stiffness testing, we conducted the impact test of a single flexible robot link. The impact experiment setup is shown in Fig. 16. The DC motor is mounted on the stage, and it is controlled by a micro-controller via a separate speed controller. An encoder[12] (1440 PPR resolution) is mounted on the output axis of the motor to monitor the position of the motor (hence the angular velocity), and the data are collected and stored in the micro-controller. The morphing arm is mounted on and driven by the DC motor. An end effector is clamped at the end of the morphing arm and controlled to hit a cargo that is placed on a frictionless slide trail.[13] A three-axis acceleration sensor[14] (0.002G resolution) is fixed on the cargo to monitor the acceleration. The acceleration data are stored by the data acquisition system. A force sensor is placed in front of the cargo to detect the impact, and the force information is monitored and stored by the micro-controller. A torpedo level[15] is used to make sure the slide trail is horizontal.

The impact test results with different stiffnesses are shown in Fig. 17. The triangle and circle line represent the acceleration of the cargo impacted by the flattened beam and curved beam (maximum deformation angle), respectively. Correspondingly, the stiffness of the compliant robotic arm is controlled with the minimum and maximum value. In this test, the impact speed is fixed as 2.2 m/s, and the sampling frequency of the sensors is set to be 500 Hz. The peaks of the associated accelerations are 45.71 m/s^2 and 56.7 m/s^2, respectively. It is observed that 19.4% decrease of the impact acceleration is obtained. With the acceleration plots, one can calculate the HIC value based on Eq. (1). The HIC values are then obtained as 150.3 m$^{5/2}$ s^{-4} and 210.3 m$^{5/2}$ s^{-4} corresponding to the configurations of minimum stiffness and maximum stiffness, respectively. The HIC value of the impact from the robot arm with minimum stiffness is 71% that from the robot arm with the maximum stiffness.

7 Discussion

From the perspective of design, the actuation four-bar linkage offers several benefits over other designs such as cable-driven systems. For instance, the toggle position enable the arm stable under the flat position. In other words, the mechanical advantage (the ratio of output over input force) is infinite in theory, which means external forces or moments cannot change the shape of the flexible beam, and only the internal torque from the motor can morph the flexible beam. Other than the toggle position, consistent electrical energy input is required from the motor to maintain a high stiffness configuration of the robot arm. This is one disadvantage of the proposed solution for stiffness tuning. It should also be noted that the design with the eight couplers and two servo motors did add complexity and mass to the system, which can compromise the benefits of variable stiffness for injury reduction in safe pHRI.

In terms of the modeling, it is observed that the stiffness model does not perfectly predict the test results and a couple of reasons are discussed as follows. The possible reasons are given below. First, the flexible beam is not ideally uniformly morphed in a curved shape. Instead, it is deformed to the desired shape on both ends of the flexible beam, which is pinned and connected to the coupler, but the flexible beam is less deformed in the middle part since there is no connections from the coupler. The nonuniform deformation may have resulted in modeling errors. In addition, the clearance of the pinned joints of the four-bar linkages also affect the accuracy of the stiffness model. Last but not the least, the 3D printed ABS beams introduce the anisotropy material property, which may result in modeling errors.

The proposed variable stiffness arm (one segment) only address the impact in the lateral direction since the stiffness of the arm is only controllable in lateral direction while other two directions are relatively rigid and not tunable. Note, the stiffness variation in the lateral direction does not affect the stiffnesses in other directions by virtue of the bearing frame design. However, an arbitrary impact force can be addressed if three tunable arms are assembled

[12]E4T 360-250-S-H-D-B, US Digital.
[13]ME-6962, PASCO.
[14]PS-2136A, PASCO.
[15]Model 43-511, Stanley.

appropriately in series. With the proper combination of the arms, the impact force with arbitrary direction can be decomposed and applied to the three links in their lateral directions correspondingly. Certainly how the robot configuration influences the effects of variable stiffness on injury reduction in an arbitrary impact direction is deemed to be an interesting future research.

This paper focuses on the design and modeling of the variable stiffness arm with a safety constraint. Obviously, in addition to stiffness, other factors such as mass of pay load, mass ratio (mass of pay load over mass of arm), impact velocity, motor torque, etc., play significant effects on the safety as well. Moreover, stiffness constant and hertz exponent (if using the nonlinear hertz contact model) are also important parameters for safety criteria. Studies of the effects of other parameters on the safety criteria are currently being conducted.

Finally, the proposed variable stiffness link design is by no means to replace the variable stiffness joint/actuator approach, but rather offers an alternative solution or complementary solution to introduce mechanical compliance to the robotic system to address the safety for physical human–robot interaction. Comparing with other variable stiffness link designs [30–32] that enable the robot link either rigid or compliant with switching mechanisms, this work developed an actively and continuously tunable stiffness arm to ensure safe and efficient operation for co-robots.

8 Conclusions

The contribution of this work is to introduce a shape morphing approach for tuning the link stiffness of a robotic arm for safe physical human–robot interactions. The PRB model method is employed for stiffness modeling, the kinematics analysis, and design optimization of the actuation mechanisms. It is found that the traditional PRB model does not accurately predict the statics of the compliant parallelogram mechanism since the clamping ends are not perfectly rigid. To address this challenge, additional torsion springs are introduced into the model, and the results show that the new model significantly improved the accuracy of the stiffness model. A 3D printed flexible robotic manipulator is designed and fabricated, and the testing results show that 3.6 times of stiffness variation and 28.57% reduction of HIC are obtained at an impact velocity of 2.2 m/s. The tests show that the feasibility to reduce impact injury by introducing compliance into the robotic link and to demonstrate the compliant link solution could be a promising approach for addressing safety concerns of physical human–robot interactions.

Acknowledgment

This material is based upon work supported by National Science Foundation (Grant No. CMMI-1637656; Funder ID: 10.13039/501100008982). Any opinions, findings, and conclusions or recommendations expressed in this material are those of the author(s) and do not necessarily reflect the views of the funding agencies.

References

[1] Colgate, E., Wannasuphoprasit, W., and Peshkin, M. A., 1996, "Cobots: Robots for Collaboration With Human Operators," International Mechanical Engineering Congress and Exhibition, Atlanta, GA, Nov. 17–22, pp. 433–439.
[2] Chu, A., Kazerooni, H., and Zoss, A., 2005, "On the Biomimetic Design of the Berkeley Lower Extremity Exoskeleton (Bleex)," IEEE International Conference on Robotics and Automation (ICRA), Barcelona, Spain, Apr. 18–22, pp. 4345–4352.
[3] Frisoli, A., Rocchi, F., Marcheschi, S., Dettori, A., Salsedo, F., and Bergamasco, M., 2005, "A New Force-Feedback Arm Exoskeleton for Haptic Interaction in Virtual Environments," First Joint Eurohaptics Conference, Symposium on Haptic Interfaces for Virtual Environment and Teleoperator Systems, World Haptics (WHC), Pisa, Italy, Mar. 18–20, pp. 195–201.
[4] Roderick, S., and Carignan, C., 2007, *Designing Safety-Critical Rehabilitation Robots*, InTech, Vienna, Austria.
[5] Wolbrecht, E. T., Chan, V., Reinkensmeyer, D. J., and Bobrow, J. E., 2008, "Optimizing Compliant, Model-Based Robotic Assistance to Promote Neurorehabilitation," IEEE Trans. Neural Syst. Rehabil. Eng., **16**(3), pp. 286–297.
[6] Yamada, Y., Konosu, H., Morizono, T., and Umetani, Y., 1999, "Proposal of Skill-Assist: A System of Assisting Human Workers by Reflecting Their Skills in Positioning Tasks," IEEE International Conference on Systems, Man, and Cybernetics, Tokyo, Japan, Oct. 12–15, Vol. 4, pp. 11–16.
[7] Kaipa, K. N., Morato, C., Liu, J., and Gupta, S. K., 2014, "Human-Robot Collaboration for Bin-Picking Tasks to Support Low-Volume Assemblies," Human-Robot Collaboration for Industrial Manufacturing Workshop, Held at Robotics: Science and Systems Conference (RSS 2014), Rome, Italy, July 16–17.
[8] Bicchi, A., Peshkin, M. A., and Colgate, J. E., 2008, "Safety for Physical Human–Robot Interaction," *Springer Handbook of Robotics*, Springer, New York, pp. 1335–1348.
[9] Versace, J., 1971, "A Review of the Severity Index," Proceedings of the 15th Stapp Conference, SAE Paper No. 710881, pp. 771–796.
[10] Newman, J. A., Shewchenko, N., and Welbourne, E., 2000, "A Proposed New Biomechanical Head Injury Assessment Function—The Maximum Power Index," Proceedings of the 44th Stapp Car Crash Conference, Atlanta, GA, SAE paper 2000-01-SC16, pp. 215–247.
[11] International Organization for Standardization, 2006, "Robots for Industrial Environments—Safety Requirements. Part I: Robot," ISO10218-1:2006.
[12] Zheng, Y.-F., and Hemami, H., 1985, "Mathematical Modeling of a Robot Collision With Its Environment," J. Rob. Syst., **2**(3), pp. 289–307.
[13] She, Y., Meng, D., Cui, J., and Su, H.-J., 2017, "On the Impact Force of Human-Robot Interaction: Joint Compliance vs. Link Compliance," 2017 IEEE International Conference on Robotics and Automation (ICRA), Marina Bay Sands, Singapore, May 29–June 3, pp. 6718–6723.
[14] Gao, D., and Wampler, C. W., 2009, "Head Injury Criterion," IEEE Rob. Autom. Mag., **16**(4), pp. 71–74.
[15] Haddadin, S., Albu-Schäffer, A., and Hirzinger, G., 2007, "Approaching Asimov's 1st Law: The Impact of the Robot's Weight Class," Robotics: Science and Systems Conference Workshop: Robot Manipulation: Sensing and Adapting the Real World (RSS2007), Atlanta, GA, June 27–30.
[16] Pervez, A., and Ryu, J., 2008, "Safe Physical Human Robot Interaction—Past, Present and Future," J. Mech. Sci. Technol., **22**(3), pp. 469–483.
[17] Iwata, H., Hoshino, H., Morita, T., and Sugano, S., 2001, "Force Detectable Surface Covers for Humanoid Robots," 2001 IEEE/ASME International Conference on Advanced Intelligent Mechatronics, Como, Italy, July 8–12, Vol. 2, pp. 1205–1210.
[18] Zinn, M., Roth, B., Khatib, O., and Salisbury, J. K., 2004, "A New Actuation Approach for Human Friendly Robot Design," Int. J. Rob. Res., **23**(4–5), pp. 379–398.
[19] Shepherd, R. F., Ilievski, F., Choi, W., Morin, S. A., Stokes, A. A., Mazzeo, A. D., Chen, X., Wang, M., and Whitesides, G. M., 2011, "Multigait Soft Robot," Proc. Natl. Acad. Sci., **108**(51), pp. 20400–20403.
[20] Tolley, M. T., Shepherd, R. F., Mosadegh, B., Galloway, K. C., Wehner, M., Karpelson, M., Wood, R. J., and Whitesides, G. M., 2014, "A Resilient, Untethered Soft Robot," Soft Robot., **1**(3), pp. 213–223.
[21] Filippini, R., Sen, S., and Bicchi, A., 2008, "Toward Soft Robots You Can Depend On," IEEE Rob. Autom. Mag., **15**(3), pp. 31–41.
[22] Ham, R. v., Sugar, T. G., Vanderborght, B., Hollander, K. W., and Lefeber, D., 2009, "Compliant Actuator Designs," IEEE Rob.Autom. Mag., **16**(3), pp. 81–94.
[23] Tsagarakis, N. G., Morfey, S., Cerda, G. M., Zhibin, L., and Caldwell, D. G., 2013, "Compliant Humanoid Coman: Optimal Joint Stiffness Tuning for Modal Frequency Control," 2013 IEEE International Conference on Robotics and Automation (ICRA), Karlsruhe, Germany, May 6–10, pp. 673–678.
[24] Pratt, G. A., and Williamson, M. M., 1995, "Series Elastic Actuators," 1995 IEEE/RSJ International Conference on Intelligent Robots and Systems. Human Robot Interaction and Cooperative Robots, Pittsburgh, PA, Aug. 5–9, Vol. 1, pp. 399–406.
[25] Haddadin, S., Albu-Schäffer, A., and Hirzinger, G., 2009, "Requirements for Safe Robots: Measurements, Analysis and New Insights," Int. J. Rob. Res., **28**(1112), pp. 1507–1527.
[26] Rodríguez, A. G., Chacón, J., Donoso, A., and Rodríguez, A. G., 2011, "Design of an Adjustable-Stiffness Spring: Mathematical Modeling and Simulation, Fabrication and Experimental Validation," Mech. Mach. Theory, **46**(12), pp. 1970–1979.
[27] Wu, Y.-S., and Lan, C.-C., 2014, "Linear Variable-Stiffness Mechanisms Based on Preloaded Curved Beams," J. Mech. Design, **136**(12), p. 122302.
[28] Ayoubi, Y., Laribi, M. A., Courrèges, F., Zeghloul, S., and Arsicault, M., 2016, "A Complete Methodology to Design a Safety Mechanism for Prismatic Joint Implementation," 2016 IEEE/RSJ International Conference on Intelligent Robots and Systems (IROS), Daejeon, South Korea, Oct. 9–14, pp. 304–309.
[29] Ayoubi, Y., Laribi, M. A., Courrèges, F., Zeghloul, S., and Arsicault, M., 2018, "Complete Design Methodology of Biomimetic Safety Device for Cobots Prismatic Joints," Rob. Auton. Syst., **102**, pp. 44–53.
[30] López-Martínez, J., Blanco-Claraco, J. L., García-Vallejo, D., and Giménez-Fernández, A., 2015, "Design and Analysis of a Flexible Linkage for Robot Safe Operation in Collaborative Scenarios," Mech. Mach. Theory, **92**, pp. 1–16.
[31] Park, J.-J., Kim, B.-S., Song, J.-B., and Kim, H.-S., 2008, "Safe Link Mechanism Based on Nonlinear Stiffness for Collision Safety," Mech. Mach. Theory, **43**(10), pp. 1332–1348.
[32] Zhang, M., Laliberté, T., and Gosselin, C., 2016, "Force Capabilities of Two-Degree-of-Freedom Serial Robots Equipped With Passive Isotropic Force Limiters," ASME J. Mech. Robot., **8**(5), p. 051002.

[33] She, Y., Su, H.-J., and Hurd, C. J., 2015, "Shape Optimization of 2D Compliant Links for Design of Inherently Safe Robots," Proceedings of IDETC/CIE, Boston, MA, Aug. 2–5, p. V05BT08A004, ASME Paper No. DETC2015-46622.
[34] She, Y., Su, H.-J., Meng, D., Song, S., and Wang, J., 2018, "Design and Modeling of a Compliant Link for Inherently Safe Corobots," J. Mech. Robot., **10**(1), p. 011001.
[35] Galloway, K. C., Clark, J. E., and Koditschek, D. E., 2013, "Variable Stiffness Legs for Robust, Efficient, and Stable Dynamic Running," J. Mech. Robot., **5**(1), p. 011009.
[36] Kim, Y.-J., Cheng, S., Kim, S., and Iagnemma, K., 2013, "A Novel Layer Jamming Mechanism With Tunable Stiffness Capability for Minimally Invasive Surgery," IEEE Trans. Rob., **29**(4), pp. 1031–1042.
[37] Hines, L., Arabagi, V., and Sitti, M., 2012, "Shape Memory Polymer-Based Flexure Stiffness Control in a Miniature Flapping-Wing Robot," IEEE Trans. Rob., **28**(4), pp. 987–990.
[38] Stilli, A., Wurdemann, H. A., and Althoefer, K., 2017, "A Novel Concept for Safe, Stiffness-Controllable Robot Links," Soft Robot., **4**(1), pp. 16–22.
[39] She, Y., 2018, "Compliant Robotic Arms for Inherently Safe Physical Human-Robot Interaction," Ph.D. thesis, The Ohio State University, Columbus, OH.
[40] Song, S., Zeng, X., She, Y., Wang, J., and Su, H.-J., 2019, "Modeling and Control of Inherently Safe Robots With Variable Stiffness Links," Rob. Auton. Syst., **120**, p. 103247.
[41] She, Y., Su, H.-J., Lai, C., and Meng, D., 2016, "Design and Prototype of a Tunable Stiffness Arm for Safe Human-Robot Interaction," Proceedings of IDETC/CIE, Charlotte, NC, Aug. 21–24, p. V05BT07A063, ASME Paper No. IDETC2016-59523.
[42] Haddadin, S., Albu-Schäffer, A., and Hirzinger, G., 2007, "Safety Evaluation of Physical Human-Robot Interaction via Crash-Testing," Robotics: Science and Systems Conference Workshop, Atlanta, GA, June 27–30, Vol. 3, pp. 217–224.
[43] Haddadin, S., Albu-Schaffer, A., and Hirzinger, G., 2008, "The Role of the Robot Mass and Velocity in Physical Human-Robot Interaction-Part I: Non-Constrained Blunt Impacts," 2008 IEEE International Conference on Robotics and Automation (ICRA), Pasadena, CA, May 19–23, pp. 1331–1338.
[44] Gao, D., and Wampler, C., 2009, "Head Injury Criterion," IEEE Rob. Autom. Mag., **16**(4), pp. 71–74.
[45] Howell, L. L., and Midha, A., 1994, "A Method for the Design of Compliant Mechanisms With Small-Length Flexural Pivots," J. Mech. Design, **116**(1), pp. 280–290.
[46] Howell, L. L., and Midha, A., 1995, "Parametric Deflection Approximations for End-Loaded, Large-Deflection Beams in Compliant Mechanisms," J. Mech. Design, **117**(1), pp. 156–165.
[47] Howell, L. L., 2001, *Compliant Mechanisms*, Wiley-Interscience, New York, NY.
[48] Waldron, K. J., Kinzel, G. L., and Agrawal, S. K., 2016, *Kinematics, Dynamics, and Design of Machinery*, John Wiley & Sons, New York, NY.